International Journal of Hydrogen Energy 142 (2025) 80–89

Contents lists available at ScienceDirect

International Journal of Hydrogen Energy

journal homepage: www.elsevier.com/locate/he

Optimal cathode design of a single high temperature PEM fuel cell: A computational study

V.K. Krastev [a,*], M. Baldelli [b], L. Bartolucci [b,**], F. Donato [c], M. Kheir Rouz [b], V. Mulone [b]

[a] Enterprise Engineering Department, University of Rome "Tor Vergata", 00133, Rome, Italy
[b] Industrial Engineering Department, University of Rome "Tor Vergata", 00133, Rome, Italy
[c] Energy Technologies Department, ENEA, Via Anguillarese 301, 00123, Rome, Italy

ARTICLE INFO

Handling Editor: Ibrahim Dincer

Keywords:
HTPEM
Fuel cell
Cathode
Flow-fields
Differential pressure
CFD

ABSTRACT

This study presents a detailed three-dimensional computational fluid dynamics (CFD) model of a single high-temperature proton exchange membrane (HTPEM) fuel cell, serving as an initial step towards the comprehensive modelling of a complete liquid-cooled fuel cell stack. The modelling framework is built to capture the complex interactions between fluid flow, heat transfer, and electrochemical reactions within the cell. Key aspects such as temperature distribution, pressure drop through channels, differential pressure across the MEA and current density distribution are analysed to understand their impact on cell performance. Results show that the cathode flow-fields design may simultaneously affect the fluid dynamics (pressure drop), MEA structural integrity and electrochemical performance of the cell.

1. Introduction

Since its early application [1–7], high-fidelity CFD modelling has been recognised as a powerful tool for the design and optimisation of PEM fuel cells. Recent literature surveys have identified 90+ Scopus-indexed publications on this topic in the 2021–2023 period only [8], thus confirming its relevance among the fuel cell research community. Although most of the available studies are oriented towards low-temperature PEM (LTPEM) applications, a significant number of CFD investigations of high-temperature PEM (HTPEM) fuel cells can be found in the scientific literature as well [1,5,6,9–22]. Compared to LTPEM, CFD modelling of HTPEM fuel cells has both advantages and additional challenges. Within the first category, we can list [12,21,23]: i) the absence of liquid water transport; ii) simplified electrochemistry modelling; iii) more straightforward temperature-dependent protonic conductivity definition in the MEA domain(s). On the other hand, the accurate description of heat generation and thermal fluxes is crucial, both during cold start-ups as well as at rated power operation [13,16,18].

The present work originates from the POR-H2 project, which has received funding from NextGeneration EU and the Italian Government for the development of R&D initiatives in the hydrogen production, transportation/storage and conversion topics. More specifically, this study covers the topic of the optimal HTPEM fuel cell stack design, with a special focus on the cathode flow-fields (gas channels). Previous CFD-based contributions on the HTPEM flow-fields design can be summarised as follows: Lobato et al. [6] compared three different cathode flow-fields geometries, neglecting explicit modelling of the anode side and showing that the 4-step serpentine and pin-type geometries perform significantly better than a straight-channel configuration. Falcucci et al. [10] took Lobato et al.'s geometries and added a triple-serpentine layout, analysing the fluid-dynamic performances of the four configurations in terms of pressure drop and reactants distribution over the active area. Xia et al. [19] focused on the channel-to-rib width ratio (CR), assuming a simplified single-channel domain both on the cathode and anode sides and finding an optimal CR range between 1 and 2. Varghese et al. [20] performed a combined CFD-FEM investigation of a single-channel HTPEM geometry, finding that the adoption of CR values above 1 might be impaired under severe GDL compression scenarios. Chowdhury and Gladen [22] analysed fluid dynamics of the cathode flow-fields for a total of 12 configurations (1 reference 4-channel serpentine plus 4 alternatives and their sub-pattern variations),

This article is part of a special issue entitled: Hydrogen Production and Transportation (Pfeifer) published in International Journal of Hydrogen Energy.

* Corresponding author.
** Corresponding author.
E-mail addresses: krastev@dii.uniroma2.it (V.K. Krastev), lorenzo.bartolucci@uniroma2.it (L. Bartolucci).

https://doi.org/10.1016/j.ijhydene.2025.05.346
Received 6 March 2025; Received in revised form 6 May 2025; Accepted 25 May 2025
Available online 3 June 2025

neglecting electrochemistry and concluding that the baseline 4-channel serpentine performs best at high load conditions, while using parallel pin-type or dual-triangle sandwich designs might be beneficial at reduced load conditions.

Compared to the literature survey listed above, the present study adds the following elements of novelty: i) full three-dimensional fluid dynamics and electrochemistry modelling of a single cell HTPEM assembly, including both cathode and anode electrodes; ii) consideration of 4 different serpentine-type cathode flow-fields and their effects on pressure drop, MEAstructural integrity and current density distribution; iii) inclusion of design and manufacturing constraints, based on the full HTPEM stack experimental activity expected within the HTPEM topic research plan under the POR-H2 funding. The remainder of the paper is organised as follows: in Section 2, the modelling framework and main geometrical features of the cell assembly are listed; Section 3 collects the main findings of the proposed computational analysis, while in Section 4 conclusions and future perspectives are briefly discussed.

2. Methodology

In this section, the governing equations and geometrical details for the full HTPEM cell model are presented. A first sub-section is dedicated to the physics and electrochemistry implemented in the cell model. The second sub-section is focused on the description of the cell assembly as well as on the different cathode design alternatives. Further details about the numerical set-up and boundary conditions will be given in Section 3.

2.1. HTPEM fuel cell model description

The HTPEM working principle is based on the classical oxy-reduction reactions of hydrogen and oxygen are considered at the anode and cathode, respectively:

$$H_2 \rightarrow 2H^+ + 2e^- \tag{1}$$

$$4H^+ + 4e^- + O_2 + N_2 \rightarrow 2H_2O + N_2. \tag{2}$$

Note that N_2 is considered in Eq. (2) since, at the cathode side, the oxidant is air and not pure oxygen. The modelling framework here presented is based on the following fundamental assumptions.

- due to the high temperatures ($T > 100$ °C), the water produced by the cathode reaction is considered to be in vapour phase;
- reactant gases (and water vapour) are considered ideal;
- due to the relatively low Reynolds number, the flow of all the species is considered in laminar conditions;
- gas diffusion layer and the catalyst layer are assumed to be homogeneous and isotropic;
- the membrane allows only for H^+ ions to pass from anode to cathode side.

2.1.1. Charge conservation

To solve the charge conservation, an electrochemistry model of anodic and cathodic reactions and ion transport is needed. For this purpose, two different potential fields are defined through their respective transport equations:

$$\nabla \cdot (\sigma_e \nabla \phi_e) + S_e = 0 \tag{3}$$

$$\nabla \cdot (\sigma_p \nabla \phi_p) + S_p = 0, \tag{4}$$

where σ_p and σ_p are the material effective electronic and protonic conductivities (S/m), ϕ_e and ϕ_p are the electric and protonic potentials (V) and S_e and S_p are the charge source terms (A/m^3) which are defined differently at the anode and cathode sides.

The source terms in Eqs. (3) and (4), can be written as a function of the volumetric current density generated at the anode (j_a) and cathode (j_c) catalyst layer:

$$S_e = -j_a \tag{5}$$

$$S_p = j_a \tag{6}$$

$$S_e = j_c \tag{7}$$

$$S_p = -j_c, \tag{8}$$

where Eqs. (5) and (6) hold in the anode catalyst layer, while Eqs. (7) and (8) hold in the cathode catalyst layer. The exchanged current density, j_a and j_c, can be evaluated using the Butler-Volmer equation:

$$j_a = \left(\zeta_a i_a^{ref} \frac{[C]_a}{[C^{ref}]_a}\right)^{\gamma_a} \left(e^{\alpha_a F \frac{\eta_a}{RT}} - e^{-\alpha_c F \frac{\eta_a}{RT}}\right) \tag{9}$$

$$j_c = \left(\zeta_c i_c^{ref} \frac{[C]_c}{[C^{ref}]_c}\right)^{\gamma_c} \left(e^{\alpha_c F \frac{\eta_c}{RT}} - e^{-\alpha_a F \frac{\eta_a}{RT}}\right), \tag{10}$$

where ζ [1/m] is the specific active surface area defined as the ratio between the surface and volume of the catalyst layer, i^{ref} [A/m^2] is the reference exchange current density, $[C]$ [kmol/m^3] are the local species concentrations. The γ and α exponents are the concentration and exchange coefficients, respectively, while η_a and η_c are the anodic and cathodic overpotentials. Finally, F, R and T, are the Faraday constant, the ideal gas constant, and the absolute temperature.

The reference exchange current density i^{ref}, can be explicitly computed as follows

$$i^{ref} = i_0^{ref} e^{-\frac{E_a}{R}\left(\frac{1}{T} - \frac{1}{T_0}\right)} \tag{11}$$

where E_a is the activation energy, i_0^{ref} is the exchange current density evaluated at the reference absolute temperature T_0. For the estimation of overpotentials η_a and η_c, the following equations hold

$$\eta_a = \phi_e - \phi_p \tag{12}$$

$$\eta_c = \phi_e - \phi_p - V_{oc} \tag{13}$$

where V_{oc} is the open circuit voltage on the cathode side.

2.1.1.1. Mass and momentum conservation. For all the gaseous fluid flows, the steady state mass conservation equation reads as follows:

$$\nabla \cdot (\rho \, \boldsymbol{u}) = S_m \tag{14}$$

Where $\boldsymbol{u}$ is the velocity vector, ρ is the mass density evaluated as the weighed mass density of each species with respect to the mass fraction of each species, and S_m is the mass source term. Together with the mass conservation, the momentum equation holds:

$$\frac{1}{\varepsilon^2} \nabla \cdot (\rho \boldsymbol{u} \, \boldsymbol{u}) = -\nabla p + \nabla \cdot \tilde{\boldsymbol{\tau}} + S_u, \tag{15}$$

where ε is the porosity of the GDL, MPL or CL, p is the pressure, $\tilde{\boldsymbol{\tau}}$ is the viscous stress tensor and $S_u = \mu/k$ is a source term related to the dynamic viscosity μ and the permeability coefficient k of the GDL, MPL and CL. Note that the function of the GDL and MPL layers in the model is the same, namely to distribute the reactants towards and remove the products from the CLs. To bridge the transition between the GDL and the CL, the structural properties of the MPL (porosity and permeability) are intermediate between the two. The source term S_m in the continuity equation is zero everywhere, with the exception of the CL, where electrochemical reactions take place. At the anode side hydrogen is

consumed to produce H^+, while at the cathode side the oxygen is consumed to produce water. The separate mass source terms can be computed as follows:

$$S_{H_2} = -\frac{PM_{H_2}}{2F} j_a \tag{16}$$

$$S_{O_2} = -\frac{PM_{O_2}}{4F} j_c \tag{17}$$

$$S_{H_2O} = \frac{PM_{H_2O}}{2F} j_c, \tag{18}$$

where PM is the molecular weight of each species and F is the Faraday constant. To ensure closure in the mass conservation equation, the mass conservation equation of each species should be considered

$$\nabla \cdot (\varepsilon \rho \boldsymbol{u} x_i) = \rho D_i^{eff} \nabla x_i + S_{m,i} \tag{19}$$

where i is the i-th species, x_i, is the mass fraction of the species and $S_{m,i}$ is one of the source terms from Eqs. (16)-(18)**, and D_i^{eff} is the effective diffusion coefficient of the i-th species in gaseous form. The latter is evaluated through a full multicomponent diffusion assumption,** Eq. (20)**, where the term $\varepsilon^{1.5}$ accounts for the porous media tortuosity, while D_{ij} and $D_{k,ij}$ are the i-th species multicomponent mass diffusivity and Knudsen diffusivity, respectively.**

$$D_i^{eff} = \frac{\varepsilon^{1.5}}{\frac{1}{D_{ij}} + \frac{1}{D_{k,ij}}} \tag{20}$$

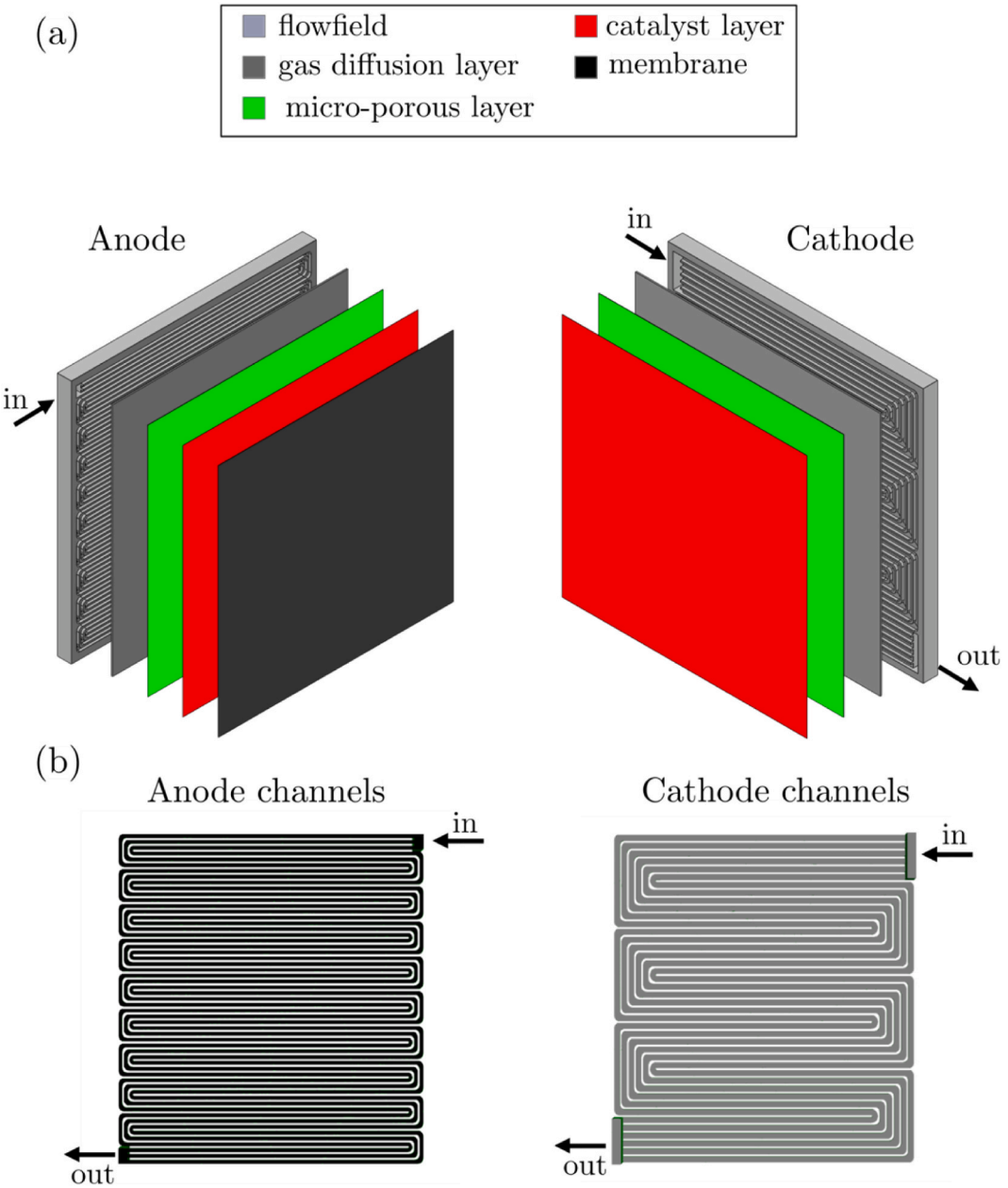

Fig. 1. Cell geometry. (a) Exploded view of the entire computational domain. The domain is composed of a pair of electrodes or BPs (light grey), GDLs (dark grey), micro-porous layers (MPLs, green), and catalyst layers (CLs, red). The central section of the domain is occupied by the PEM (black). **(b)** Frontal view of the anode (left) and one of the cathode (right) channel configuration (D4). (For interpretation of the references to colour in this figure legend, the reader is referred to the Web version of this article.)

2.1.2. Energy conservation

The last conservation equation represents the conservation of energy:

$$\nabla \cdot (\boldsymbol{u}(\rho E + p)) = \nabla \cdot \left(\lambda_{eff} \nabla T - \sum_i h_i \boldsymbol{J}_i + \tilde{\boldsymbol{\tau}} \cdot \boldsymbol{u} \right) + S_h \quad (21)$$

where E is the energy content of the gas mixture, λ_{eff} is the effective thermal conductivity of the gas in a porous media, h_i and $J_i = D_i \nabla x_i$ are the enthalpy and the flux vector of the i-th species, respectively. Finally, S_h is the thermal source due to the irreversibilities in the electrochemical reactions.

Discretization and solution of all the governing equations is performed through the Finite Volume Method (FVM) within the ANSYS® Fluent CFD code, using a second-order steady-state solution scheme with coupled pressure-velocity correction [24,25].

2.2. Geometries

Fig. 1(a) shows a detailed representation of each part of the computational domain, while in Table 1 the overall size and geometry details of the single cell MEA and BPs are provided. Note that the MEA characteristics are derived from the BASF Celtec® P1100W MEA [26], which is going to be used in the upcoming POR-H2 experimental activity. For the flow-fields design, a total of four cathode configurations and a single anode configuration have been considered (see Table 2). The cathode design alternatives include triple (D1-D3) and 6-step (D4) serpentine channels, with different cross sections and channel-to-rib-ratios, while the anode design is a triple serpentine with a 0.49 mm^2 single channel square cross-section.

The serpentine-like design pattern was selected as it is generally known to be a good compromise between pressure drop and reactant distribution efficiency. The variation range of the channel and rib geometrical parameters follows manufacturing constraints, set up by the facility that will produce the graphite-based BPs needed for the POR-H2 experimental campaign. Finally, the serpentine arrangement allows for all design variants provision for cooling channels in the full cell stack configuration.

3. Results & discussion

3.1. Reference polarisation curve

To correctly reproduce the polarisation curve of the Celtec® P1100W MEA, the parameters included in Eqs. (9) and (10) must be calibrated against single cell data with similar serpentine-type channels and under relevant operating conditions. For this purpose, the triple-serpentine configuration modelled in Ref. [21] and experimentally investigated in Ref. [5] has been taken as a reference and compared against the D1 cell design. The cell operating conditions are reported in Table 3, where the reference current density i_m is used to calculate the reactants inlet massflows according to the equation:

$$\dot{m}_i = \frac{\xi_i M_i}{F n_i} \, i_m A \quad (22)$$

Table 1
HTPEM numerical domain size.

Parameters	Description	Value
A	MEA active area	45 cm^2 (6.72 × 6.72)
A_{BP}	BP area included in the domain	49 cm^2 (7 × 7)
H_{BP}	BP thickness	4 mm
H_{CL}	CL thickness	10 μm
H_{GDL}	GDL thickness	350 μm
H_M	Membrane thickness	75 μm
H_{MPL}	MPL thickness	65 μm

Table 2
Flow-fields design alternatives.

Parameters	Description	D1 (3x)	D2 (3x)	D3 (3x)	D4 (6x)
CR_c	Channel/rib ratio (cathode)	1.6	2.4	3.25	2.4
CR_c/CR_a	–	1.07	1.6	2.17	1.6
S_c	Cathode channel section	0.56 mm^2 (0.8 × 0.7)	0.84 mm^2 (1.2 × 0.7)	0.91 mm^2 (1.3 × 0.7)	0.84 mm^2 (1.2 × 0.7)
$S_{c,tot}$	Cathode total section	1.68 mm^2	2.52 mm^2	2.73 mm^2	5.04 mm^2
$S_{c,tot}/S_{a,tot}$	–	1.14	1.73	1.81	3.42

Table 3
Reference cell operating conditions.

Parameters	Description	Anode	Cathode
i_m	Reference current density	1 A/cm^2	
ξ	Reactants stoichiometry	1.2 (H_2)	2 (air)
RH	Relative humidity (ambient)	10 %	30 %
$\dot{m}$	Inlet mass flows	5.75×10^{-7} kg/s	3.25×10^{-5} kg/s
T_n	Cell nominal temperature	160 °C	
p_{out}	Reactants outlet pressure	1 atm	
T_{in}	Reactants inlet temperature	120 °C	

where M is the molecular weight, F is the Faraday constant and n is the oxi-reduction reaction coefficient ($n_{H_2} = 2$ and $n_{O_2} = 4$). Note that Eq. (21) is valid only for pure hydrogen and oxygen streams and thus has to be adjusted for the actual reactant composition.

The electrochemistry parameters used by the ANSYS® Fluent PEMFC model are shown in Table 4, where the value of the protonic conductivity has been calculated at the cell's nominal temperature according to the equation proposed in Ref. [21].

In terms of numerical boundary conditions, massflow inlets and pressure outlets are imposed at the gas channels inflow/outflow boundaries. All external walls are treated as adiabatic, except for the anode/cathode terminals where a constant temperature equal to the cell's nominal operating temperature is set. A total of 4 computational grids have been evaluated for the spatial discretization of the D1 geometry, ranging from 3.8 M to 8.5 M cells. Details from the coarsest and finest generated meshes are given in Table 5, highlighting a +120 % increase in the element count, as well as a −20 % and −95 % (a factor of 20) decrease in the minimum and maximum cell volumes, respectively. Fig. 2 gives a visual representation of the coarsest and finest refinement in the cathode oxidant channels.

To check if the coarsest mesh level is enough for a good representation of the fuel cell key performance parameters, a side-by-side comparison has been made with the finest mesh. Fig. 3 displays current density and cathode pressure drop results, for a cell rated voltage of 0.5

Table 4
Electrochemistry parameters used in the simulations.

Parameters	Description	Anode	Cathode
i_0^{ref}	Ref. Exchange current density	2200 A/m^2	0.0033 A/m^2
ζ	Specific active surface area	10^7	2×10^7
$[C^{ref}]$	Reference molar concentration	0.04088 kmol/m^3	0.04088 kmol/m^3
γ	Concentration exponent	0.5	1
α_a	Exchange exponent (anode)	0.5	0.45
α_c	Exchange exponent (cathode)	0.5	0.45
V_0	Reversible potential	0 V	1.152 V
ΔS	Entropy of formation	0 J/kmolK	−44330 J/kmolK
σ_p	Membrane/CL protonic conductivity	8.65 S/m	

Table 5
Details of the coarsest and finest D1 meshes.

	D1 - Coarsest	D1 - Finest
Total n. of elements	3835274	8536577
Tetras	87.5 %	84.4 %
Hexas	11 %	14.4 %
Pyramids	1.5 %	1.2 %
Min. Element volume	1.12×10^{-8} mm^3	8.83×10^{-9} mm^3
Max. Element volume	1.37×10^{-3} mm^3	2.45×10-^{4} mm^3

V. For both parameters, the difference between the two meshes is within 4 %, thus confirming that the coarsest level is an acceptable compromise between accuracy and computational efficiency. Simulations reported from now on are all performed at the coarsest mesh level, for all the considered cell designs.

The polarisation curve sweep is performed changing the cell voltage at constant reactants mass flow rates.

Fig. 4 shows the comparison between the D1 polarisation curve and the reference from literature. There is a very good agreement in the ohmic losses region, while there are some discrepancies in the activation losses region at low current densities.

Overall, the model behaviour is satisfactory, considering the actual differences between the D1 design and the reference. More in details, the reference cell is smaller (25 cm^2 vs 45 cm^2) and features larger cathode channels; the currently investigated layout therefore exhibits a longer reactant path and slightly higher activation losses at very low current densities (<0.15 A cm-2). Nevertheless, these geometric differences do not influence the accuracy of the model in the voltage range of practical interest. Indeed, HTPEM stacks commonly operates at a rated cell voltage around 0.5–0.6 V [26], which is well into the ohmic region where the deviation between numerical results and experimental reference is less than 2 %.

3.2. *Effects of cathode flow-fields design*

For a thorough comparison between the four proposed cathode

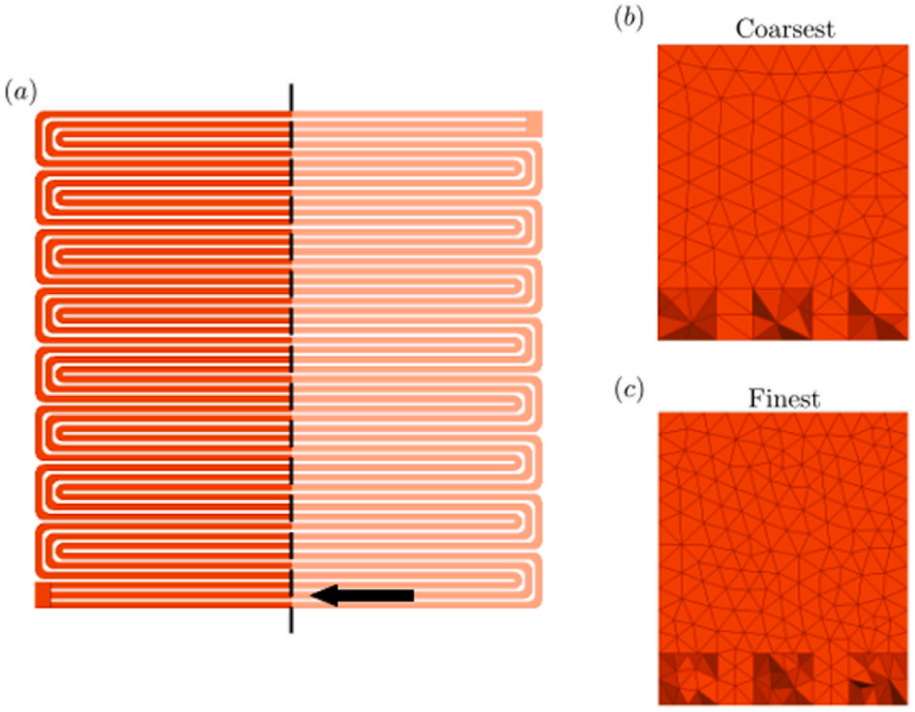

Fig. 2. Coarsest vs. Finest D1 mesh details. **(a)** domain cut-out; **(b)** coarsest mesh; **(c)** finest mesh.

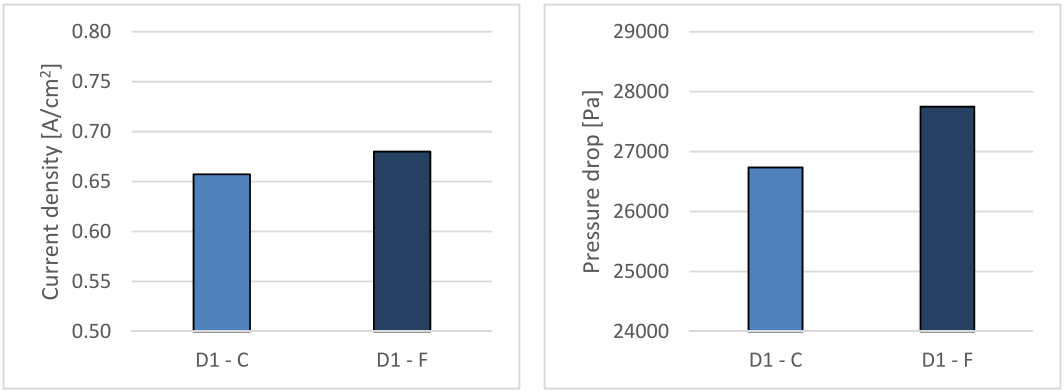

Fig. 3. Coarsest vs. Finest D1 mesh comparison. **(a)** MEA current density and **(b)** pressure drop at the cathode flow-fields.

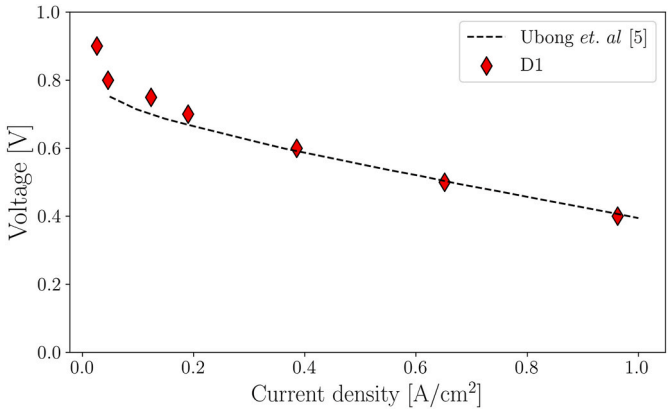

Fig. 4. Polarisation curve for D1, T_n = 160 °C. Comparison with the reference data [5].

designs, the reference case has been slightly modified, to better resemble actual thermal management at rated operating conditions. Specifically, instead of the uniform fixed temperature BC, a simplified cooling ramp has been imposed at the anode/cathode terminals (Fig. 5). The ramp assumes a 5 °C coolant temperature difference and an average coolant temperature of 155 °C, thus 5 °C below the nominal cell temperature. All other simulation parameters are as already listed in the previous subsection, while the comparison has been made at a rated cell voltage of 0.5 V.

3.2.1. *Pressure distribution in flow-fields*

A fundamental output parameter from the simulations is the flow-fields pressure distribution, which is crucial for the cell efficiency (pressure drop within the channels) and the MEA structural integrity (local differential pressure acting on the membrane).

Fig. 6 shows cathode-side pressure drops and cathode vs. anode pressure drop ratios. The D1 case produces a cathode pressure drop around 0.26 bar, which is about 10 times higher than the equivalent pressure drop at the anode side and is not acceptable at the given flow rates. To achieve comparable pressure drops at the cathode and anode sides, the overall gas passage section should be at least 3 times larger at the cathode (D4).

For the evaluation of the differential pressure, a membrane integrity index (MII) has been defined as follows:

$$MII = \frac{p_{cat} - \overline{p}_{an}}{0.13 \cdot 10^5} \tag{23}$$

where p_{cat} is the local pressure at the membrane-CL interface on the cathode side, $\overline{p}_{an}$ is the average pressure acting on the membrane on the anode side and 0.13 bar is the maximum local differential pressure allowed for the safe operation of the Celtec® P1100W MEA.

To preserve the membrane integrity, the MII value must be well below unity across the membrane surface. Fig. 7 shows the MII contour distribution for all cathode designs, highlighting critically high MII values on a large portion of the membrane area for the D1 case. For D2 and D3 there is a significant reduction in the MI average magnitude, but the maximum values are still too close to 1 (~0.8) for a safe MEA operation. On the other hand, the D4 design guarantees very low MII values (below 0.4) on the whole membrane surface.

Current flux density distribution & polarisation curves.

Fig. 8 shows the average current density and the current density uniformity index (UI) for the four considered designs.

The UI index represents how a specified field variable varies over a surface, where a value of 1 indicates the highest uniformity [24,25]. Fig. 8(a) highlights a higher current output for D1, but the analysis of Figs. 9 and 10 indicates that the actual reason for that is not a better reactant utilisation efficiency. In fact, the much higher overpressure generated at the cathode side alters (increases) the oxygen concentration across most of the serpentine pattern (Fig. 10(a)), thus augmenting the volumetric current production at the CL. Fig. 8(b) shows instead that the D4 cases produces the best uniformity of current density distribution among all the considered designs, which is also visually confirmed by Fig. 9(b). A more uniform current distribution is desirable to reduce thermal stresses and thus mitigate the membrane deterioration over time.

Finally, Fig. 11 collects polarisation curves for all the considered cathode designs, in the 0.4–0.9 V range. Within the cell's useful voltage range (0.4–0.6 V), the maximum difference in the current output is less than 6 % for the two limiting designs. The difference between the D4 design and the two intermediate D2 and D4 designs does not exceed 3.5 % in the same range. These findings further support the choice of D4 as the optimal cathode flow-fields design, due to MEA safety and current uniformity arguments, with only very limited losses in the overall current output.

3.3. *Practical design guidelines*

The single-cell simulations allow the derivation of quantitative targets that can be used directly in the preliminary design of HT-PEMFC stacks. Table 6 summarises the recommended limits together with the corresponding engineering actions.

3.3.1. *Robustness and scalability*

- **Pressure-drop scaling.** In laminar regime, Δp scales linearly with channel length and inversely with the cube of the hydraulic diameter; thus, if cross-section and number of passes are preserved, the Δ

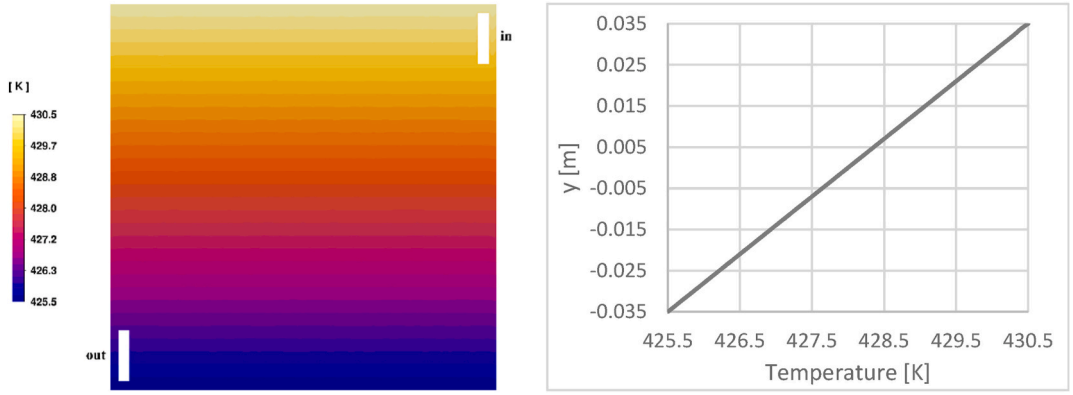

Fig. 5. Simplified temperature ramp imposed at the anode and cathode terminals.

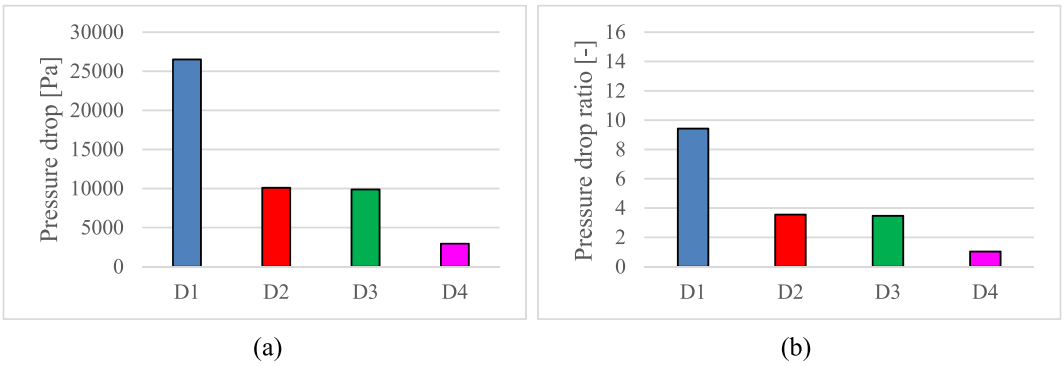

Fig. 6. **(a)** cathode pressure drop and **(b)** cathode vs. anode pressure drop ratio for the four considered cathode designs.

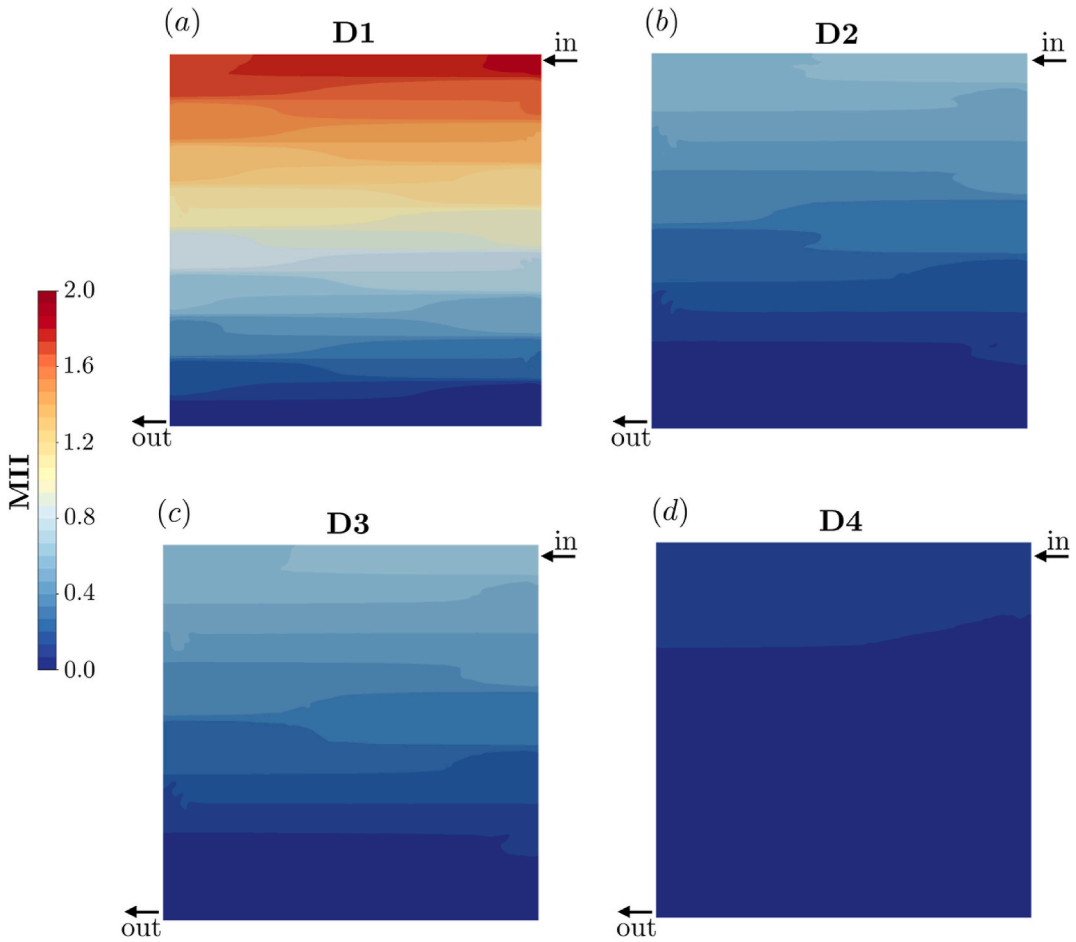

Fig. 7. Membrane Integrity Index, cathode catalyst-membrane interface.

$p_c/\Delta p_a$ ratio remains essentially constant when the active area grows from 45 cm^2 to ≥150 cm^2 [8].

- **Manifold distribution.** Experimental measurements on ten-cell HT-PEM stacks equipped with six-pass flow-fields report cell-to-cell pressure spreads <5 kPa, demonstrating that the single-cell flow-field can be extrapolated to the stack without loss of hydraulic balance [27].

These independent sources support the robustness of the proposed criteria and confirm that the six-pass (*D4*) serpentine pattern retains its hydraulic, electrochemical, and structural integrity advantages when applied to multi-cell stacks.

4. Conclusions

The design-oriented single cell simulations presented in the previous Section have provided valuable insights for the realisation of the HTPEM experimental stack within the POR-H2 research project.

More in details, the following conclusions can be drawn.

- to ensure structural integrity of the MEA and achieve reasonable overpressure at the cathode side, an adequate global passage section should be provided through the flow-fields (at least 3 times higher than the anode flow-fields section): this favours a 6-step serpentine design for the cathode flow-fields, compared to the baseline triple-serpentine configuration;

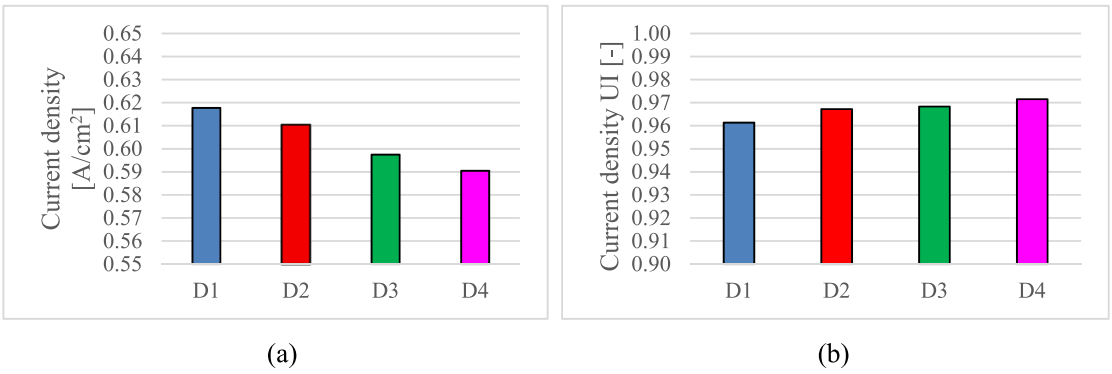

Fig. 8. (a) Average MEA current density **(b)** current density Uniformity Index, cathode catalyst-membrane interface.

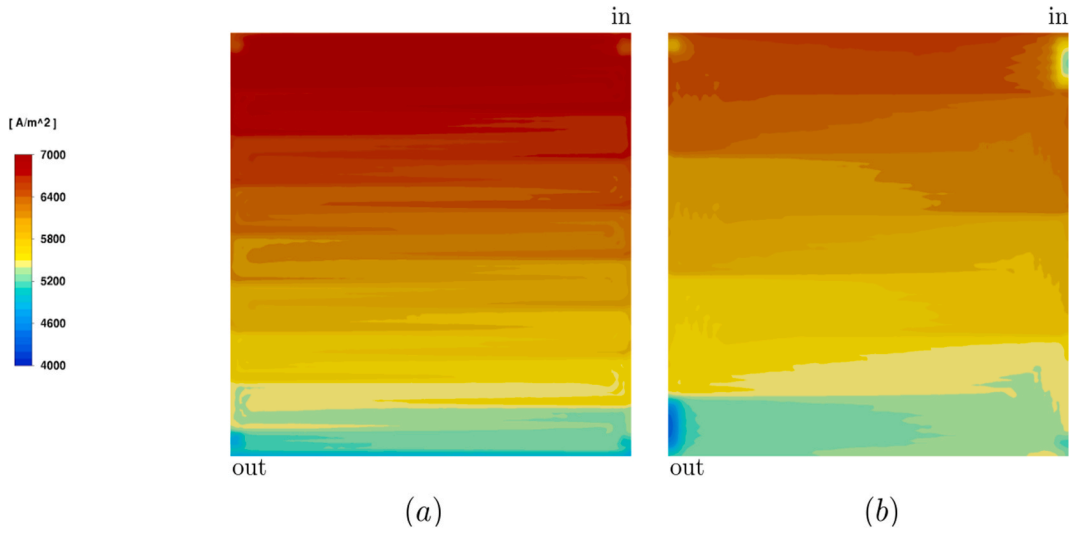

Fig. 9. Current flux density distribution. (a) cathode catalyst-membrane interface, D1; **(b)** cathode catalyst-membrane interface, D4.

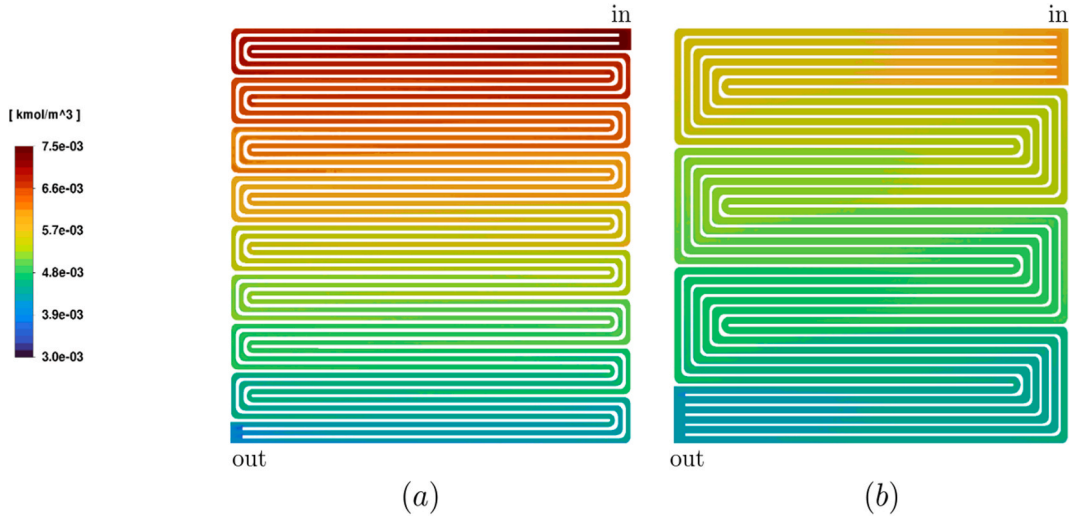

Fig. 10. O_2 molar concentration. (a) cathode flow-fields, D1; **(b)** cathode flow-fields, D4.

- lower pressure losses (and thus lower gas velocities) guarantee a more uniform oxidant distribution along the cathode flow-fields, with consequently better oxidant utilisation;
- an improvement in the uniformity of the current density distribution is directly linked with smaller temperature gradients and, therefore, longer duration of the MEA.

The optimal, 6-step cathode serpentine design will be adopted in the

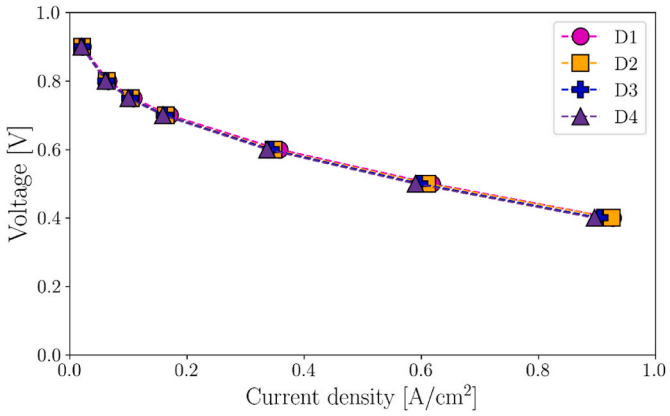

Fig. 11. Polarisation curves for all cathode designs.

Table 6
Details of the quantitative design targets derived from the simulations.

Design target	Quantitative criterion	Actionable rule for the stack
Pressure-drop balance	$\Delta p_c/\Delta p_a \approx 1 \pm 0.2$	Provide a total cathode flow area $\geq 3\times$ anode flow area; six-pass serpentine with 1.2 × 0.7 mm channels (5.0 mm^2 per pass).
Membrane integrity	MII <0.4 everywhere	Keep the local *trans*-membrane Δp below 0.13 bar by adopting wider cathode channels and limiting GDL compression.
Current-density uniformity	Uniformity index >0.95	Gas velocity <2 m s^{-1} and multi-pass serpentine layout.

manufacturing of the forthcoming experimental stack. Next steps of the computational modelling research activity will include: i) the insertion of liquid cooling channels integrated within the graphite BPs; ii) the realisation of a full stack three-dimensional model (up to 5 cells) with cooling channels; iii) a simulation campaign dedicated to the stack thermal management strategy optimisation.

CRediT authorship contribution statement

V.K. Krastev: Writing – original draft, Investigation, Conceptualization. **M. Baldelli:** Writing – original draft, Conceptualization. **L. Bartolucci:** Software, Formal analysis, Conceptualization. **F. Donato:** Supervision, Funding acquisition, Conceptualization. **M. Kheir Rouz:** Supervision, Methodology, Conceptualization. **V. Mulone:** Supervision, Funding acquisition, Conceptualization.

Declaration of competing interest

The authors declare that they have no known competing financial interests or personal relationships that could have appeared to influence the work reported in this paper.

Acknowledgments

This research has been funded by the European Union – NextGeneration EU and by the Italian Ministry of Environment and Energy Security, POR H2 AdP MEES/ENEA with involvement of CNR and RSE, PNRR - Mission 2, Component 2, Investment 3.5 "Ricerca e sviluppo sull'idrogeno" WP 3.1 LA 3.1.4 "Gestione e validazione dell'ingegneria di stack di celle a combustibile a membrana polimerica".

References

[1] Peng J, Lee SJ. Numerical simulation of proton exchange membrane fuel cells at high operating temperature. J Power Sources 2006;162:1182–91. https://doi.org/10.1016/j.jpowsour.2006.08.001.
[2] Ferng YM, Su A. A three-dimensional full-cell CFD model used to investigate the effects of different flow channel designs on PEMFC performance. Int J Hydrogen Energy 2007;32:4466–76. https://doi.org/10.1016/j.ijhydene.2007.05.012.
[3] Jang JH, Yan WM, Li HY, Tsai WC. Three-dimensional numerical study on cell performance and transport phenomena of PEM fuel cells with conventional flow fields. Int J Hydrogen Energy 2008;33:156–64. https://doi.org/10.1016/j.ijhydene.2007.09.005.
[4] Rismanchi B, Akbari MH. Performance prediction of proton exchange membrane fuel cells using a three-dimensional model. Int J Hydrogen Energy 2008;33:439–48. https://doi.org/10.1016/j.ijhydene.2007.07.046.
[5] Ubong EU, Shi Z, Wang X. Three-dimensional modeling and experimental study of a high temperature PBI-based PEM fuel cell. J Electrochem Soc 2009;156:B1276. https://doi.org/10.1149/1.3203309.
[6] Lobato J, Cañizares P, Rodrigo MA, Pinar FJ, Mena E, Úbeda D. Three-dimensional model of a 50 cm2 high temperature PEM fuel cell. Study of the flow channel geometry influence. Int J Hydrogen Energy 2010;35:5510–20. https://doi.org/10.1016/j.ijhydene.2010.02.089.
[7] Cordiner S, Mulone V, Romanelli F. Thermal-fluid-dynamic simulation of a proton exchange membrane fuel cell using a hierarchical 3D-1D approach. J. Fuel Cell Sci. Technol. 2007;4(3):317–27. https://doi.org/10.1115/1.2744052.
[8] Edwards H, Pereira MP, Gharaie S, Omrani R, Shabani B. Computational fluid dynamics modelling of proton exchange membrane fuel cells: accuracy and time efficiency. Int J Hydrogen Energy 2024;50:682–710. https://doi.org/10.1016/j.ijhydene.2023.09.004.
[9] Siegel C, Bandlamudi G, Heinzel A. Systematic characterization of a PBI/H3PO4 sol-gel membrane - modeling and simulation. J Power Sources 2011;196:2735–49. https://doi.org/10.1016/j.jpowsour.2010.11.028.
[10] Falcucci G, Jannelli E, Minutillo M, Ubertini S. Fluid dynamic investigation of channel design in high temperature PEM fuel cells. J Fuel Cell Sci Technol 2012;9. https://doi.org/10.1115/1.4005628.
[11] Krastev VK, Falcucci G, Jannelli E, Minutillo M, Cozzolino R. 3D CFD modeling and experimental characterization of HT PEM fuel cells at different anode gas compositions. Int J Hydrogen Energy 2014;39. https://doi.org/10.1016/j.ijhydene.2014.09.015.
[12] Yin Y, Wang J, Yang X, Du Q, Fang J, Jiao K. Modeling of high temperature proton exchange membrane fuel cells with novel sulfonated polybenzimidazole membranes. Int J Hydrogen Energy 2014;39:13671–80. https://doi.org/10.1016/j.ijhydene.2014.04.019.
[13] Reddy EH, Jayanti S, Monder DS. Thermal management of high temperature polymer electrolyte membrane fuel cell stacks in the power range of 1-10 kWe. Int J Hydrogen Energy 2014;39:20127–38. https://doi.org/10.1016/j.ijhydene.2014.09.132.
[14] Bezmalinović D, Strahl S, Roda V, Husar A. Water transport study in a high temperature proton exchange membrane fuel cell stack. Int J Hydrogen Energy 2014;39:10627–40. https://doi.org/10.1016/j.ijhydene.2014.04.186.
[15] Krastev VK, Falcucci G. On the detailed multidimensional modeling of HT PEM fuell cells and stacks. In: AIP conf proc; 2015. https://doi.org/10.1063/1.4912792.
[16] Huang H, Zhou Y, Deng H, Xie X, Du Q, Yin Y, Jiao K. Modeling of high temperature proton exchange membrane fuel cell start-up processes. Int J Hydrogen Energy 2016;41:3113–27. https://doi.org/10.1016/j.ijhydene.2015.12.134.
[17] Caglayan DG, Sezgin B, Devrim Y, Eroglu I. Three-dimensional non-isothermal model development of high temperature PEM Fuel Cells. Int J Hydrogen Energy 2018;43:10834–41. https://doi.org/10.1016/j.ijhydene.2018.01.176.
[18] Varghese G, V, Babu KP, Joseph TV, Chippar P. A numerical investigation on thermal gradients and stresses in high temperature PEM fuel cell during start-up. Int J Heat Mass Tran 2021;175. https://doi.org/10.1016/j.ijheatmasstransfer.2021.121365.
[19] Xia L, Xu Q, He Q, Ni M, Seng M. Numerical study of high temperature proton exchange membrane fuel cell (HT-PEMFC) with a focus on rib design. Int J Hydrogen Energy 2021;46:21098–111. https://doi.org/10.1016/j.ijhydene.2021.03.192.
[20] Varghese G, Venkatesh VB, Joseph TV, Chippar P. Combined effect of channel to rib width ratio and gas diffusion layer deformation on high temperature – polymer electrolyte membrane fuel cell performance. Int J Hydrogen Energy 2022;47:33014–26. https://doi.org/10.1016/j.ijhydene.2022.07.178.
[21] Wang J, Wang S, Zhu Y, Wang Y. Effect of cooling surface temperature difference on the performance of high-temperature PEMFCs. Int J Hydrogen Energy 2023;48:16813–28. https://doi.org/10.1016/j.ijhydene.2023.01.125.
[22] Chowdhury PR, Gladen AC. Design of flow fields for high-temperature PEM fuel cells using computational fluid dynamics. Energies 2024;17. https://doi.org/10.3390/en17194898.
[23] Abdul Rasheed RK, Liao Q, Caizhi Z, Chan SH. A review on modelling of high temperature proton exchange membrane fuel cells (HT-PEMFCs). Int J Hydrogen Energy 2017;42:3142–65. https://doi.org/10.1016/j.ijhydene.2016.10.078.
[24] Ansys Inc. ANSYS® academic research CFD, release 2024 R1. Fluent User's Guide; 2024. http://www.ansys.com.

[25] Ansys Inc. ANSYS® academic research CFD, release 2024 R1. Fluent Theory Guide; 2024. http://www.ansys.com.
[26] J. Song, BASF Stack Handbook How to build, test, and diagnose high temperature PEM fuel cell stacks with Celtec ® P1100W, in: E. De Castro, S. Yu (Eds.), BASF Fuel Cell, Inc., n.d. www.fuel-cell.basf.com.
[27] Lee CY, Weng FB, Kuo YW, Tsai CH, Cheng YT, Cheng CK, Lin JT. In-situ measurement of high-temperature proton exchange membrane fuel cell stack using flexible five-in-one micro-sensor. Sensors (Switzerland) 2016;16. https://doi.org/10.3390/s16101731.